

Observations of ubiquitous compressive waves in the Sun's chromosphere

Richard J. Morton¹, Gary Verth¹

Solar Physics and Space Plasma Research Centre (SP²RC), The University of Sheffield, Hicks Building, Hounsfield Road, Sheffield S3 7RH, UK

David B. Jess², David Kuridze²

Astrophysics Research Centre, School of Mathematics and Physics, Queens University, Belfast, BT7 1NN, UK.

Michael S. Ruderman¹, Mihalis Mathioudakis², Robertus Erélyi^{*1}

Received / Accepted

ABSTRACT

The details of the mechanism(s) responsible for the observed heating and dynamics of the solar atmosphere still remain a mystery. Magnetohydrodynamic (MHD) waves are thought to play a vital role in this process. Although it has been shown that incompressible waves are ubiquitous in off-limb solar atmospheric observations their energy cannot be readily dissipated. We provide here, for the first time, on-disk observation and identification of concurrent MHD wave modes, both compressible and incompressible, in the solar chromosphere. The observed ubiquity and estimated energy flux associated with the detected MHD waves suggest the chromosphere is a vast reservoir of wave energy with the potential to meet chromospheric and coronal heating requirements. We are also able to propose an upper bound on the flux of the observed wave energy that is able to reach the corona based on observational constraints, which has important implications for the suggested mechanism(s) for quiescent coronal heating.

*To whom correspondence should be addressed. Email: robertus@sheffield.ac.uk

Subject headings: Sun: Chromosphere, Sun: Corona, Waves, MHD

1. Introduction

The quiet chromosphere is a highly dynamic region of the Sun's atmosphere. It consists of many small-scale, short-lived, magnetic flux tubes (MFTs) composed of relatively cool (10^4 K) plasma [1]. The quiet chromosphere may be divided into two magnetically distinct regions [2]. One is the

network, which generally consists of open magnetic fields outlined by plasma jets, i.e., spicules and mottles, which protrude into the hot (10^6 K) corona. The other region is the inter-network that is populated by fibrils that outline magnetic fields, joining regions of opposite polarity hence are closed within the chromosphere [1,3,4]. The possible importance of chromospheric dynamics on the upper atmosphere has recently been highlighted by joint Hinode and Solar Dynamic Observatory (SDO) [5] and ground-based observations by the Swedish Solar Telescope [6] showing a direct correspondence between chromospheric structures and plasma that is heated to coronal temperatures.

Magnetohydrodynamic (MHD) waves have long been a suggested mechanism for distributing magneto-convective energy, generated below the solar surface, to the upper layers of the Sun’s atmosphere [7,8]. Incompressible MHD wave modes, characterised by the transverse motions of the magnetic field lines, have been observed to be ubiquitous throughout the solar chromosphere [9-11] and corona [12-14]. However, incompressible wave energy is notoriously difficult to dissipate under solar atmospheric conditions [5] requiring very large Alfvén speed gradients occurring over short (sub-resolution) spatial scales to achieve the necessary rate of plasma heating.

In contrast, compressible MHD waves are readily dissipated by, e.g., compressive viscosity and thermal conduction [15]. Active region fast compressible MHD waves have recently been identified at both photospheric and coronal heights [16-18]. There has been some tentative evidence for their existence in the quiet chromosphere [19] but now we establish their ubiquity in this paper, making them a possible candidate for plasma heating in the quiescent corona.

We demonstrate here the presence of concurrent, ubiquitous, fast compressive MHD waves and incompressible MHD waves in the on-disk solar chromosphere. Measurements of the wave properties (i.e., period, amplitude, phase speed) for both compressible and incompressible modes are provided. Further, we derive estimates for the flux of wave energy by combining advanced MHD wave theory and the observed wave properties. These estimates hint that the observed waves could play a crucial role in the transport of magneto-convective energy in the solar atmosphere.

2. Results

2.1. The chromospheric fine structure

High spatial (150 km) and temporal resolution (8 s) observations with the Rapid Oscillations in the Solar Atmosphere (ROSA) imager [20] have allowed us to resolve the chromospheric structures and measure fine-scale wave-like motions therein. The data are obtained close to disk centre with a narrowband 0.25 \AA $H\alpha$ core (6562.8 \AA) filter on the 29 September 2010 (see Methods for further information on the processing of the observational data). The field of view covers a $34 \text{ Mm} \times 34 \text{ Mm}$ region of the typical quiet Sun (Fig. 1, Supplementary Fig. S1). The $H\alpha$ core images are known to show the mid- to upper chromosphere where the magnetic pressure dominates the gas pressure [3,21]. The images (Supplementary Movie S1) show that the on-disk chromosphere is dominated by

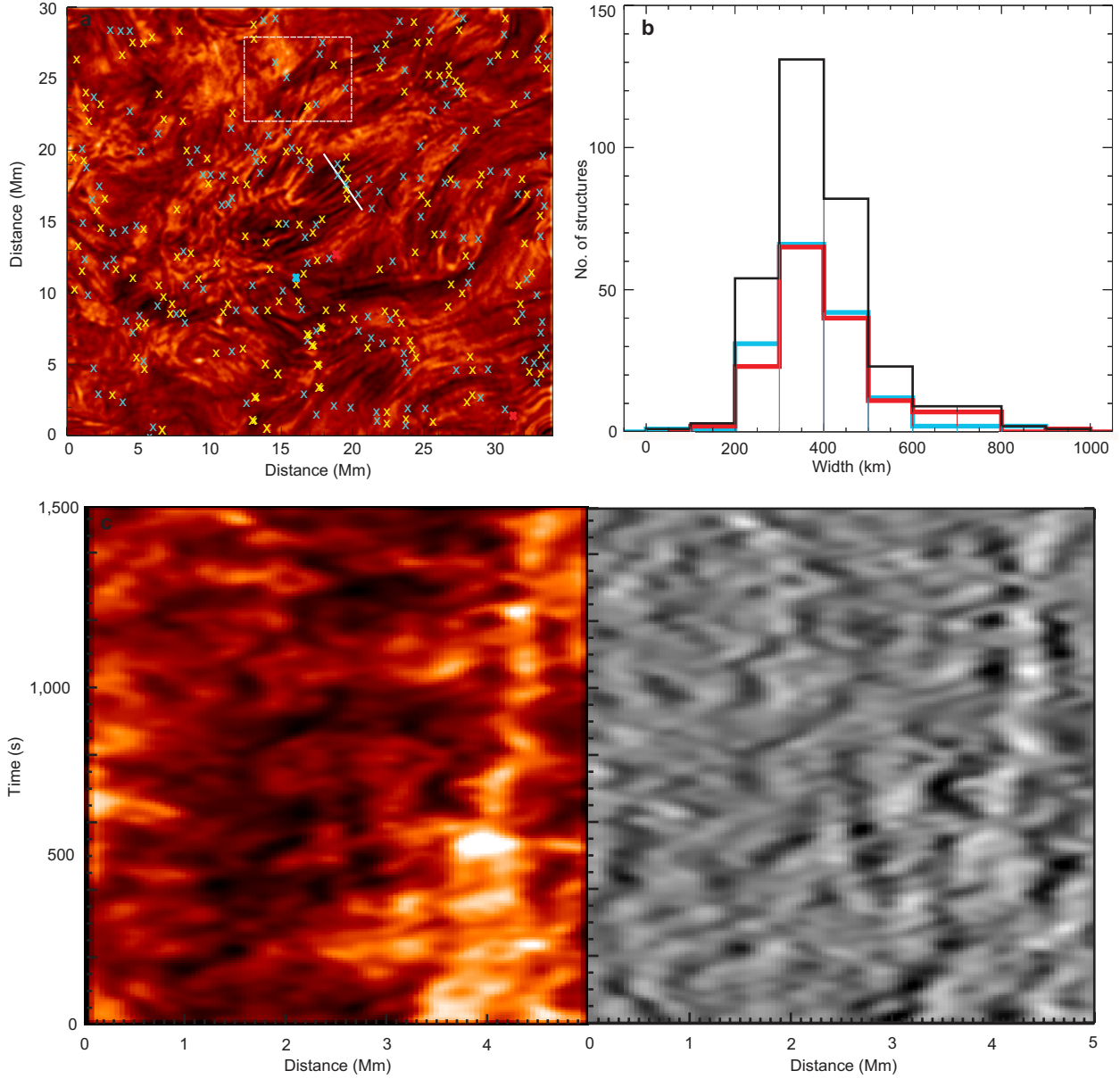


Fig. 1.— Observed chromospheric structures and their transverse motions. (a) The ROSA H field of view at $t=0$ s. Blue and yellow crosses mark positions of identified dark and white chromospheric MFTs, respectively. The boxed region is where the chromospheric structures in Fig. 4 are observed. (b) Histogram of measured MFT widths. Blue and red lines correspond to the dark and bright MFTs, respectively. The black line is the combined result with a mean width of 360 ± 120 km. (c) Time-distance plot (left) and median filtered version (right) taken across a group of chromospheric structures. The cross-cut used is shown in (a). The given distance starts from the bottom of the cross-cut and the time is in seconds from the beginning of the data set. The dark and white linear tracks are the transverse motions of the structures.

hundreds of bright and dark fine structures, all displaying highly dynamic behaviour. The elongated structures are the fibrils and shorter structures are the mottles. Recent advances in the modelling of H α line formation suggest the dark structures are regions of enhanced density that closely follow the magnetic field structure [22]. The nature of the bright fine structures are less clear, although they are suspected to be similar to the dark features except for differences in their gas pressure [23]. In Fig.1 we show the measured widths of over 300 bright and dark structures, and the results demonstrate the geometric similarity between these structures.

The observed structures can be considered as discrete over-dense MFTs outlining the magnetic field, embedded in a less dense ambient plasma. They are short lived (1-5 minutes) but fortunately survive long enough to allow measurements of important wave parameters, e.g., velocity amplitude and propagation speed. The observations show that similar structures re-occur in the same regions either continuously or even tens of minutes after previous structures have faded from the field of view (Supplementary Movies S1 and S2), suggesting that the lifetime of the background magnetic field is much longer than the plasma flows that generate the visible structuring.

Waves may be present in the atmosphere even when the magnetic field is not outlined by an intensity enhancement; however, they are far more difficult to identify directly. These intensity enhancements suggest a greater plasma density along the waveguide relative to the surrounding atmosphere, which has important physical effects on the properties of the wave. Mathematically, it is well known that plasma structuring in solar waveguides, even if modelled as relatively simple over-dense cylindrical MFTs, can produce an infinite set of orthogonal eigenmodes [24,25]. This is in stark contrast to only three possible modes of a homogeneous magnetized plasma (Alfvén, fast and slow magnetosonic modes). Although the full MHD spectrum of permitted wave modes in realistic inhomogeneous solar MFTs is rich and complex, in practice, due to limits in spatial resolution, most of the wave power observed so far has been confined to the low order azimuthal wave number modes, i.e., torsional Alfvén, sausage and kink. Higher order fluting modes predicted by theory, to our knowledge, have yet to be detected in solar data. It has, however, been suggested by numerical simulations that different MHD wave modes should occur simultaneously in chromospheric MFTs [26]. In this current work, we identify such concurrent wave modes.

2.2. Incompressible transverse waves

To analyse the waves, a cross-cut is placed perpendicular to a chromospheric structures axis and time- distance plots are constructed (e.g., Fig. 1, Supplementary Figs. S2, S3). We find that the chromospheric structures support two concurrent orthogonal MHD wave modes. The first type is the transverse motion of the structures axis (Fig. 2), which is ubiquitous and even visible by eye (Supplementary Movies S1-S4). In terms of the over-dense magnetic waveguide model we interpret these motions as the highly incompressible MHD fast kink wave [24,25]. The transverse displacements appear predominantly as linear, diagonal tracks in the time-distance plots, although occasionally leaving sinusoidal tracks (see Methods for further details). The properties of

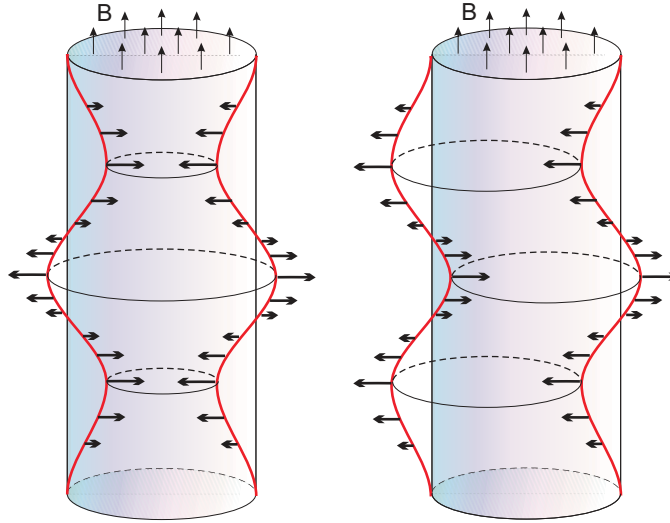


Fig. 2.— Schematic diagrams of MHD waves in a magnetic flux tube. The MHD wave modes supported by the chromospheric fine structure can be modelled as a cylindrical magnetic waveguide. The fast MHD sausage wave (left) is characterised by a periodic contraction and expansion of the MFTs cross-section symmetric about the central axis, stretching and squeezing the magnetic field. This, in turn, induces a decrease and increase in the plasma pressure inside the MFT that changes the intensity of the observed MFT in the H bandpass. The fast MHD kink wave (right) displaces the central axis of the MFT. The red lines show the perturbed waveguide and thick arrows show the velocity amplitudes. The thin arrows labelled B show the direction of the background magnetic field.

over a hundred representative transverse motions were measured and they reveal that the typical displacement amplitudes are 315 ± 130 km with velocity amplitudes of $5\text{-}15$ km s^{-1} (Fig. 3). For isolated chromospheric structures (e.g., those in Fig. 4 and Supplementary Fig. S2) a Gaussian can be reliably fitted to the cross-sectional flux profile to obtain the transverse displacement and velocity amplitudes, and the period (see Methods for further details). A linear fit to the diagonal tracks is undertaken when a Gaussian fit cannot be performed. The number of structures to which a Gaussian fit can be applied is 47; the remainder of the fits are linear. Using cross-correlation, the propagation speeds can also be measured and values in the range $40\text{-}130$ km s^{-1} are obtained (Supplementary Table S1). We note that the amplitude and period of the waves observed here are similar to those reported in limb observations of spicules [10]. The amplitudes of the transverse motions are of the order of, or greater than, the waveguide width (360 km), implying that they are fast kink wave modes in the non-linear regime.

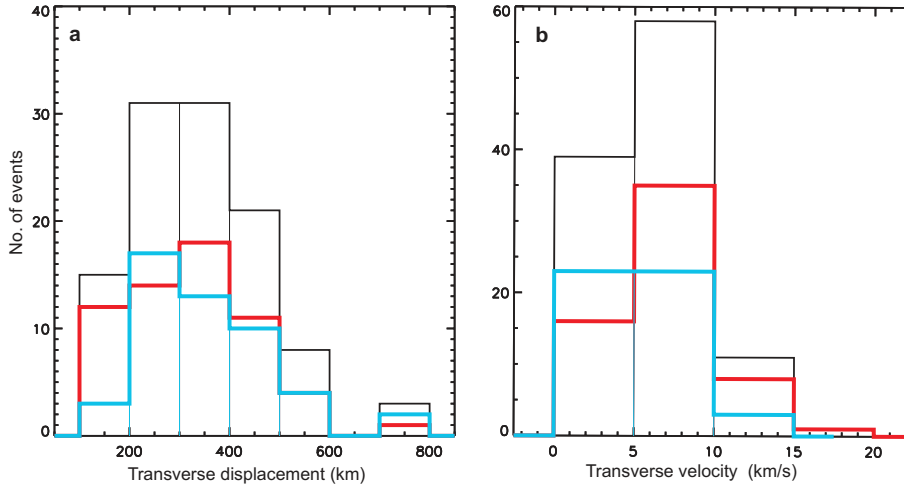


Fig. 3.— Measured properties of transverse displacements and velocity amplitudes for the fast MHD kink mode. (a) The distribution of transverse displacements of 103 chromospheric structures measured using linear fits to the observed tracks. The blue and red lines correspond to dark and bright structures, respectively. The black line shows the combined results with a mean displacement of 315 km and standard deviation of 130 km. (b) Velocity amplitudes for both bright and dark chromospheric structures. The transverse velocity has a mean value of 6.4 km s^{-1} with a standard deviation of 2.8 km s^{-1} . The dark and bright structures show a similar distribution.

2.3. Fast compressible waves

The second type of dynamic behaviour in chromospheric structures (Fig. 2), concurrent with the transverse displacement (Figs. 4, 5, Supplementary Figs. S2, S4), is a periodic increase and decrease of the structures intensity. In conjunction, there is an anti-correlated contraction and expansion of the structures visible cross-section. Both the intensity and width perturbations are obtained from the Gaussian fits. This perturbation is found to propagate along chromospheric structures with speeds much greater than the sound speed and is comparable to the local Alfvén speed (see Methods for further details). We interpret the observed periodic changes in intensity from MHD wave theory [24,25] as being consistent with the compressive properties of the fast MHD sausage mode. The visible lifetime of the chromospheric structures are also comparable to the fast sausage and kink modes period, which means that observing multiple wave cycles is rather difficult. However, the fast propagating intensity disturbances can also be identified in time-distance diagrams that are constructed when a cross-cut is placed parallel to a structures axis (see, Fig. 5, Supplementary Figs. S4, S5, S6). These events are seen to occur continuously all over the field of view (Supplementary Movies S3 and S4). A table of measured phase speeds and periods are provided in Supplementary Table S2.

Interestingly, the sausage mode has distinct regimes that define whether the majority of wave energy can be trapped in the vicinity of a density enhancement along the magnetic field or it

leaks away [24,25,27]. To investigate whether the observed fast MHD sausage modes are mostly trapped or leaky we have to estimate if the product of wavenumber (k) and waveguide half-width (a) is a sufficiently small parameter. For the observed chromospheric structures the sausage mode would have to have $ka > 0.2$ to be trapped but we observe, e.g., for the example in Fig. 4, that $ka \sim 0.08 \pm 0.03$ (see Supplementary Information for further details). Therefore, the observed sausage modes appear to be in the leaky regime, further enhancing their already dissipative nature. It is important to note that leaky sausage modes, with no damping due to physical effects such as compressive viscosity or radiation, would still radiate energy away from the waveguide with decay times on the order of the period.

Now, let us estimate the energy flux for the observed MHD waves using the waveguide model. The polarisation relations for a particular wave mode allow us to determine the perturbations of all the relevant physical quantities, if we know the perturbation of one [24,25]. This way we obtain an estimate for the amplitude of the perturbations we cannot measure directly otherwise, e.g. the magnetic field fluctuations (see Supplementary Information for further details). The polarisation relations need to be supplemented with typical values of chromospheric plasma parameters (e.g., density [1,22], $\rho = 3 \times 10^{-10}$ kg/m³, temperature [22,23], $T = 10,000$ K and magnetic field strength [28], $B = 10 - 30$ Tesla) and the amplitudes and phase speeds measured here. The time-averaged wave energy flux in the chromospheric plasma is composed of two dominant components, the kinetic and the magnetic energy flux, $\langle E \rangle = c_{ph}[\rho v^2 + b^2/\mu_0]/4$, where v and b are the amplitudes of the velocity and magnetic perturbations, respectively, c_{ph} is the phase speed and μ_0 is the magnetic permeability of free space. The thermal energy contributions from each mode are found to be negligible due to the magnetic pressure being at least an order of magnitude greater than the gas pressure in the chromosphere. The estimated energy flux of the incompressible fast kink mode is $\langle E_k \rangle = 4300 \pm 2700$ W/m², which is comparable to that estimated in off-limb spicules [9,10]. The estimated wave energy flux for the compressible fast MHD sausage mode is $\langle E_s \rangle = 11700 \pm 3800$ W/m² per chromospheric structure for apparent radial velocity amplitudes of $v \sim 1 - 2$ km s⁻¹. The details of the wave energy calculation applicable to the observed inhomogeneous structured plasma are given in the Supplementary Methods, Supplementary Figs. S7, S8 and Supplementary Table S3.

A further comment on the wave energy flux is required. The over-dense cylindrical waveguide supports different MHD wave modes, where some of the energy of trapped modes is concentrated near the waveguide. Consequently, the consideration of collections of over-dense waveguides occupying the chromosphere results in a much more complex calculation of the total energy flux. The derived value does not take into account the following: The wave energy of leaky modes is not confined within the flux tube, with a comparable amount of perturbation energy outside the tube. This means calculation of the internal wave energy flux only, leads to an underestimate; Only a linear approach for the wave energy flux is given. The transverse motions are generally observed to be strongly non-linear, so we are underestimating the wave energy flux by ignoring these non-linear terms; The true nature of the chromospheric fine structure is difficult to determine

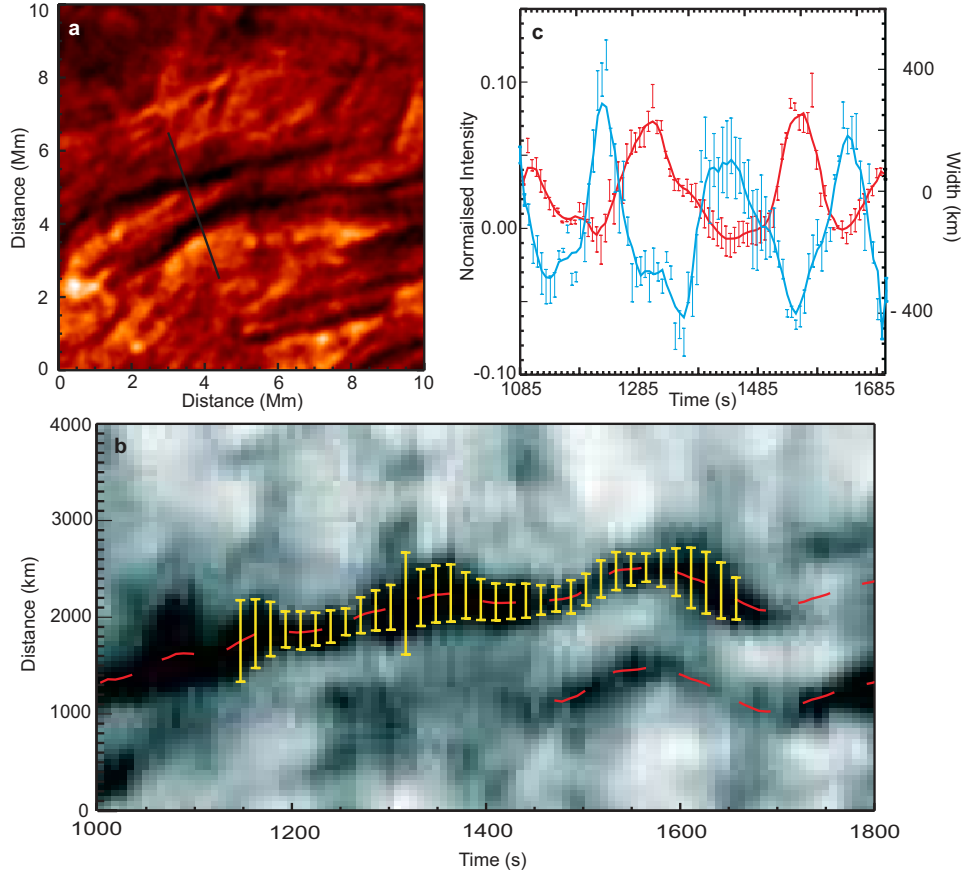


Fig. 4.— Concurrent wave modes in chromospheric structures. (a) Typical ROSA H α example of a pair of relatively large dark flux tubes at $t = 1536$ s measured from the beginning of the data series. (b) Time- distance plot revealing the dynamic motion. The position of the cross-cut is shown in (a), with the given distance starting at the top of the cross-cut. Times are given in seconds from the start of the data set. The results from a Gaussian fitting are over-plotted and show the non-linear fast MHD kink wave (red line shows the central axis of the structure) and the fast MHD sausage mode (yellow bars show the measured width of structure). The transverse motion has a period of 232 ± 8 s and we detect multi- directional propagating transversal wave trains in the MFT travelling with speeds of 71 ± 22 km s $^{-1}$ upwards and 87 ± 26 km s $^{-1}$ downwards (for further details see, Supplementary Fig. S6). The typical velocity amplitudes are 5 km s $^{-1}$. The fast MHD sausage mode has a period of 197 ± 8 s, a phase speed of 67 ± 15 km s $^{-1}$ and apparent velocity amplitudes of 1 – 2 km s $^{-1}$ (c) Comparison of MFTs intensity (blue) and width (red) perturbations from the Gaussian fitting. The data points have been fitted with a smoothed 3-point box-car function. The observed out-of-phase behaviour is typical of fast MHD sausage waves. The error bars plotted are the one-sigma errors on each value calculated from the Gaussian fitting.

at present. The homogeneous cylindrical model is a simplifying assumption and does not account

for the true geometry of the structure and/or any radial structuring of the plasma. All the above factors could influence the energy estimates. Calculating the total wave energy in a plasma such as the chromosphere is complex and will require further observations and full 3-dimensional MHD numerical simulations before improved values for wave energy flux can be obtained.

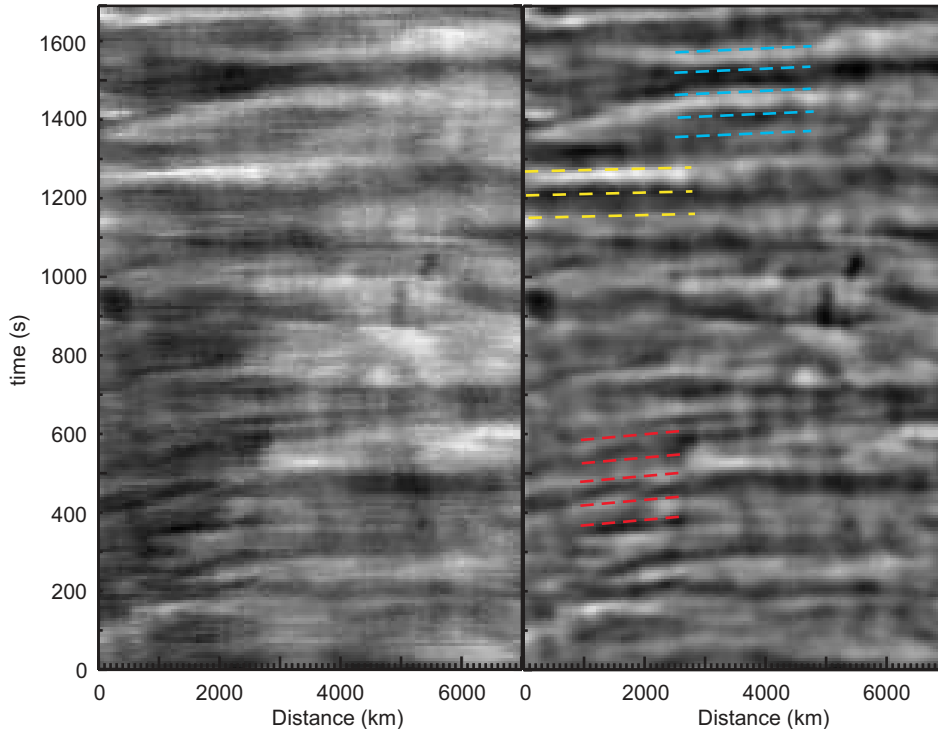


Fig. 5.— Fast propagating intensity perturbations (a) A typical time-distance diagram obtained by placing a cross-cut parallel to a chromospheric structure. This particular cross-cut is perpendicular to the cross-cut shown in Fig. 1a. (b) The same time-distance plot is shown as in (a) but it has been subject to a high-pass Atrous filter. The result reveals periodic variations in intensity that propagate along the cross-cut, hence the chromospheric structure. Measuring the gradients of the tracks created by the intensity perturbations across the time-distance plots provides propagation velocities. The coloured, dashed lines highlight three examples of these periodic variations. The measured propagation velocities are $78 \pm 9 \text{ km s}^{-1}$ (red), $270 \pm 135 \text{ km s}^{-1}$ (yellow) and $135 \pm 17 \text{ km s}^{-1}$ (blue). The amplitude of the perturbation in intensity is $\leq 10\%$ of the background value, similar to that found from the Gaussian fitting (Fig. 4).

3. Discussion

Knowing the eventual fate of the wave energy observed in the chromosphere is vital in assessing which (if any) wave-based heating models are likely candidates for explaining the long-standing solar atmospheric heating puzzle [29-35]. Using the measured properties of the chromospheric structures,

we estimate (see Supplementary Information for further details) that a maximum of 4 – 5% of the chromospheric volume is connected by MFTs that protrude into the corona. This estimate of connectivity between the chromosphere and corona is subject to observational constraints but the given value may not change significantly with improved spatial resolution.

The estimated connectivity suggests that the total energy flux across the solar surface able to reach the corona from the chromosphere is $\sim 170 \pm 110 \text{ W/m}^{-2}$ for the incompressible transverse motions and $\sim 460 \pm 150 \text{ W/m}^2$ for compressive motions. The estimate for chromospheric transverse wave energy able to reach the lower corona agrees with the energy estimates in the same period range (100-500 s) from off-limb SDO quiet Sun observations [14], which could suggest that these waves remain relatively undamped on their journey. This can be explained by the known difficulty of dissipating these incompressible waves [15]. Since it is expected that the majority of field lines observed here remain closed (i.e., the fibrillar structure), this suggests that the observed chromospheric wave energy remains largely in the chromospheric volume to be dissipated in a different manner [33-35]. On the other hand, the eventual fate of the chromospheric fast compressive waves is still unclear. However, our results imply that the waves could play a significant role in meeting chromospheric ($\sim 10 \text{ kW/m}^2$ [36]) and quiet coronal heating requirements (100–200 W/m^2 [36,37]). Further work is needed to: provide more representative statistics on typical perturbation amplitudes of the fast compressive waves, which will lead to improved estimates for the energy flux of the waves; search for coronal counterparts of the sausage MHD waves in the corona; and assess how the leaky nature of the waves affects the wave energy transmission to and dissipation in the lower corona.

The observations presented here demonstrate that the on-disk quiet chromosphere, which is dominated by fibrillar structure, supports ubiquitous incompressible transverse waves. The properties of the transverse waves observed agree with those reported to exist in limb spicules [10], which are magnetic waveguides that penetrate into the low corona. This points towards a close connection between the disk and limb structures even if their magnetic topology (i.e., open or closed magnetic fields) is potentially different. In addition, the observation and identification of ubiquitous, fast propagating, compressible MHD waves demonstrate that the chromosphere is replete with MHD wave energy. The ubiquity of both the incompressible and compressible waves, in conjunction with our initial estimates of wave energy, gives further credence to models of a predominantly wave-based quiescent atmospheric heating mechanism.

4. Methods

4.1. Observational set-up and data processing

The data was obtained at 15:41-16:51 UT on 29 September 2010 with the Dunn Solar Telescope at Sacramento Peak, USA. The six-camera system Rapid Oscillations in the Solar Atmosphere (ROSA) was employed. ROSA observed a 69.3 by 69.3 region of the quiet solar atmosphere in

Hydrogen α (6562.7 Å). The H α filter is centred at the line core and a narrow bandpass (0.25 Å) is employed to ensure that photospheric contributions from the line wings are minimised (for details on H α line formation see, e.g., [refs. 3, 21, 22]). During the observations, high-order adaptive optics [38] were used to correct for wave front deformation in real time. The seeing conditions were good. The data suffers from a period of poor seeing during the middle of the run lasting 300 s. The frames in this period of bad seeing are not used for analysis. The H α data was sampled at 2.075 frames s⁻¹ and image quality improved through speckle reconstruction [39] utilising a 161 ratio, giving a final cadence of 7.68 s. To ensure accurate co- alignment between frames, the narrowband time series were Fourier co-registered and de-stretched using vectors derived from longer-lived broadband structures [40].

4.2. Gaussian fitting of chromospheric structures

We discuss here the procedure used to observe the periodic phenomena in the chromospheric magnetic structures. First, we place cross-cuts perpendicular to the structures central axis and obtain time- distance diagrams as shown in Figs. 1, 4 and Supplementary Fig. S2. In each time slice, t , of the time- distance plot we fit a Gaussian profile to the cross-sectional flux profile, $F(x, t)$, of the chromospheric magnetic structure, where the Gaussian fit is given by

$$F_{fit}(x, t) = f_0(t) \exp\left(-\frac{(x - f_1(t))^2}{2f_2^2(t)}\right) + f_3(t) \quad (1)$$

Here, $f_0(t)$ is the peak flux, $f_1(t)$ is the central position of the Gaussian, $f_2(t)$ is the Gaussian width and $f_3(t)$ is the background flux. The obtained fit parameters relate to the periodic motions: $f_0(t)$ gives intensity (or flux) perturbation; $f_1(t)$ gives the displacement of the structures central axis, i.e., the transverse waves; $f_2(t)$ gives the full-width half-maximum (FWHM), $FWHM = 2f_2\sqrt{2\ln 2}$, of the structures visible cross-section. Before measuring the properties (e.g., period, velocity amplitude, etc.) of each series f_0, f_1, \dots , each time series is de-trend by fitting a cubic function and subtracting the trend. The periods of the wave motion are obtained by using wavelet analysis. Examples of structures demonstrating periodic phenomenon derived from the Gaussian fits are shown in Fig. 4 and Supplementary Fig. S1. The Gaussian fit is applied only to isolated chromospheric flux tubes to avoid the influence of the chromospheric structures crossing each other, which would lead to changes in both intensity and width. All errors provided with respect to the results obtained from the Gaussian fitting (i.e., those in Fig. 4, Supplementary Table S1) are one standard deviation.

4.3. Measuring transverse amplitudes

Here we discuss how the transverse amplitudes are obtained for the histograms in Fig. 3. In the time- distance diagrams a large number of diagonal tracks (Fig. 1, Supplementary Fig. S3),

with varying gradients, and a smaller number of sinusoidal tracks (e.g., Fig 4, Supplementary Fig. S2) can be identified. These are the transverse motions of the chromospheric structures. The transverse amplitudes are obtained by measuring the length of the bright or dark diagonal tracks and the time averaged velocity amplitudes are the gradients of the tracks. The Gaussian fit is not used here for determining the centre of the chromospheric structure. The spatial position of the centre of the chromospheric structures can be measured to the nearest pixel by locating the maximum/minimum value of intensity, which provides an error of 50 km on position. The time coordinate for each position of the chromospheric structure can only be known to within a range of 7.68 s, hence the error is $dt \pm 3.84$ s. For the measured values of displacement amplitude given in Fig. 3 the median value of the error is $\sim 13\%$ of the given value. The velocity amplitude has a median error of 22 % of the given value, which equates to 1.3 km s^{-1} and a standard deviation on the error of 1.1 km s^{-1} .

Calculating the velocity amplitude from the straight line fits only provides the time-averaged value of the amplitude. If a number of oscillatory cycles can be observed, then the following relation is used to find the maximum velocity amplitude,

$$v_r = \frac{\partial \xi_r}{\partial t} = \frac{2\pi}{P\xi_r} \quad (2)$$

Here ξ_r is the transverse displacement (given by f_1 in the Gaussian fit), v_r is the radial velocity perturbation and P is the period of the oscillation. Only a small percentage of the observed oscillations show full cycles, i.e., sinusoidal motions in the time-distance plots. The reason why we do not see full cycles is due to the relatively short lifetimes (1-5 minutes) of the chromospheric magnetic structures compared to a typical period of the fast kink waves (3 minutes). A similar behaviour is observed for limb spicules [9,10].

4.4. Amplitudes of the fast MHD sausage mode

Here we describe how we estimate the velocity component of the fast MHD sausage mode from the changes in the FWHM as established by the Gaussian fitting outlined in the Methods section in the main paper. We assume that the compressive motion is a symmetric perturbation about the central axis of the waveguide. The FWHM is a measure of the chromospheric structures visible diameter. We make the assumption that the displacement in the radial direction occurs at the same rate as the change in the value of the FWHM. The radial velocity amplitude is given by Equation 2 and we assume $\xi_r \propto FWHM/2$. Equation 2 can only be used when a number of cycles of the fast sausage mode are observed. The value for v_r is the value of maximum amplitude. The time-averaged value is given by $\langle v_r \rangle = v_r/\sqrt{2}$. We note that the assumption regarding the relationship between FWHM and the radial velocity may not hold true if the change in the visible cross-section does not accurately represent the physical change in cross-section. Detailed simulations of waves in plasmas and their influence on H α line formation may be needed to resolve such issues.

4.5. Fast propagating intensity disturbances

The spatial resolution of ROSA (~ 150 km) is close to the widths of the chromospheric flux tubes (~ 350 km), making the joint detection of periodic changes in intensity and the width of flux tubes difficult to observe. However, it is possible to identify the fast compressive wave mode through identification of periodic, propagating intensity disturbances (Fig. 5, Supplementary Fig. S4, S6). The intensity variations seen in the filtered data is $\leq 10\%$ of the median intensity of the unfiltered intensity. This variation in intensity is in agreement with the values obtained from the Gaussian fits (compare Fig. 4 and Supplementary Fig. S2). From these filtered time-distance plots we are able to measure propagation speeds and periods of the observed periodic disturbances (see Supplementary Table S2). We identify 10 regions in which the properties of the fast propagating features can be measured (Supplementary Fig. S6).

We are confident the observed perturbations are due to the fast sausage modes as the periodic features have a large spatial coherence (> 1000 km - see Supplementary Movies S3 and S4). This behaviour is somewhat expected due to the leaky nature of the oscillations (see Supplementary Information for further details). In contrast, the observed kink motions have a small spatial coherence (see, Fig. 1), with neighbouring flux tubes showing little or no coherence.

4.6. Measuring phase speeds

To measure the phase speed for the observed waves in chromospheric structures, we have to be able to track the periodic variation in, i.e., displacement, intensity, at different positions along the structure. We place cross-cuts at different positions along the structures central axis and fit a Gaussian to the observed sinusoidal variations. The time lag between the perturbed quantities obtained from the Gaussian fit in the different cross-cuts is obtained by using cross-correlation to calculate the shift between two signals. The phase speed is given as the average velocity determined from the time lags between different cross-cuts (see Supplementary Information for further details) and the error is the standard deviation.

The propagating nature of the waves is also seen by plotting the transverse displacement for different cross-cuts (as measured with the Gaussian fits). An example of this is shown in Supplementary Fig. S5, where the propagation of the transverse wave shown in Fig. 4 can be seen. The distance between the displayed cross-cuts is ~ 150 km. We note that it is possible that the phase speed varies as a function of distance along the structure due to density and magnetic field stratification; however, a combination of the technique used and the spatial and temporal resolution of the current observations does not allow us to determine this variation of phase speed.

The phase speeds for the fast compressive disturbances are calculated differently. Once a periodic propagating disturbance is identified in time-distance plot (e.g., Fig. 5, Supplementary Fig. 4), the minimum or maximum valued pixel in time (depending on whether the maximum or

minimum of the intensity perturbation is being measured) in each spatial slice is located. The gradient of a linear fit to the minimum/maximum values gives the phase speed. The errors on the spatial locations are 50 km and the time coordinates are 3.84 s. As the propagating disturbances are seen over relatively long distances for short periods of time, the largest source of error comes from the uncertainty in time.

5. References and Notes:

1. Beckers, J. Solar spicules. *Sol. Phys.* 2, 367-433 (1968)
2. Dowdy, J., Rabin, D., Moore, R. On the magnetic structure of the quiet transition region. *Sol. Phys.* 105, 35-45 (1986)
3. Rutten, R., The quiet-Sun photosphere and chromosphere, *Phil. Trans. Roy. Soc A*, 370, 3129-3150 (2012)
4. Schrijver, C. et al. Large-scale coronal heating by the small-scale magnetic field of the Sun. *Nature* 394, 152-154 (1998)
5. De Pontieu, B. et al. The origins of hot plasma in the solar corona. *Science* 331, 55-58 (2011)
6. Wedemeyer-Bhm, S. et al. Magnetic tornadoes as energy channels into the solar corona. *Nature*, 486, 505-508 (2012)
7. Schatzman, E. The heating of the solar corona and chromosphere. *Annal. d'Astrphys.* 12, 203-218 (1949)
8. Osterbrock, D. The heating of the solar chromosphere, plages and corona by magnetohydrodynamic waves. *Astrophys. J.* 134, 347-388 (1961)
9. De Pontieu, B. et al. Chromospheric Alfvénic waves strong enough to power the solar wind. *Science* 318, 1574-1577 (2007)
10. Okamoto, T., De Pontieu, B. Propagating waves along spicules. *Astrophys. J.* 736, L24 (2011)
11. Jess, D. et al. Alfvén waves in the lower solar atmosphere. *Science* 323, 1582-1585 (2009)
12. Tomczyk, S. et al. Alfvén waves in the quiet solar corona. *Science* 317, 1192-1196 (2007)
13. Erdlyi, R., Taroyan, Y. Hinode EUV spectroscopic observations of coronal oscillations. *Astron. Astrophys.* 489, L49 (2008)
14. McIntosh, S. et al. Alfvénic waves with sufficient energy to power the quiet solar corona and fast solar wind. *Nature* 475, 477-480 (2011)
15. Braginskii, S. Transport Processes in a Plasma. *Rev. Plasma Phys.* 1, 205 (1965)
16. Morton, R., Erdlyi, R., Jess, D., Mathiudakis, M. Observations of sausage modes in magnetic pores. *Astrophys. J.* 729, L18 (2011)
17. Liu, W. et al. Direct Imaging of Quasi-periodic Fast Propagating Waves of 2000 km s⁻¹ in the Low Solar Corona by the Solar Dynamics Observatory Atmospheric Imaging Assembly. *Astrophys. J.* 736, L13 (2011)
18. Shen, Y., Liu, Y. Observational study of the quasi-periodic fast propagating magnetosonic waves and the associated flare on 2011 May 30. *Astrophys. J.* 753, 53 (2012)
19. Jess, D. et al. The origin of type-I spicule oscillations. *Astrophys. J.* 744, L5 (2012)

20. Jess, D. et al. ROSA: A high-cadence, synchronized multi-camera system. *Sol. Phys.* 261, 363-373 (2010)
21. Leenaarts, J. et al. DOT tomography of the solar atmosphere VI: Magnetic elements as bright points in the blue wing. *Astron. Astrophys.* 449, 1209-1218 (2006)
22. Leenaarts, J., Carlsson, M., van der Voort, L., The formation of the H line in the solar chromosphere, 749, 136 (2012)
23. Heinzel, P., Schmieder, B. Chromospheric fine structure: black and white mottles. *Astron. Astrophys.* 282, 939-954 (1994)
24. Spruit, H. Propagation speeds and acoustic damping of waves in magnetic flux tubes. *Sol. Phys.* 75, 3-17 (1982)
25. Edwin, P., Roberts, B. Wave propagation in a magnetic cylinder. *Sol. Phys.* 88, 179-191 (1983)
26. Fedun, V., Sheytag, S., Erdlyi, R. Numerical modelling of footpoint-driven magneto-acoustic wave propagation in a localized solar flux tube. *Astrophys. J.* 727, 17 (2011)
27. Cally, P. Leaky and non-leaky oscillations in magnetic flux tubes, *Sol. Phys.* 103, 277-298 (1986)
28. Trujillo-Bueno, J. et al. The Hanle and Zeeman effects in solar spicules: a novel diagnostic window on chromospheric magnetism. *Astrophys. J.* 619, L191-L194 (2005).
29. Ionson, J. Resonant absorption of alfvénic surface wave and the heating of solar coronal loops. *Astrophys. J.* 226, 650-673 (1978)
30. Hollweg, J. Resonances of coronal loops. *Astrophys. J.* 277, 392-403 (1984)
31. Poedts, S., Goossens, M., Kerner, W. Numerical simulation of coronal heating by resonant absorption of Alfvén waves. *Sol. Phys.* 123, 83-115 (1989)
32. Ruderman, M., Berghmans, D., Goossens, M., Poedts, S. Direct excitation of resonant torsional Alfvén wave by footpoint motions. *Astron. Astrophys.* 320, 305-318 (1997)
33. Matthaeus, W. et al. Coronal heating by magnetohydrodynamic turbulence driven by reflected low-frequency waves. *Astrophys. J.* 523, L93-L96 (1999)
34. Cranmer, S., van Ballegoijen, A., Edgar, R. Self-consistent coronal heating and solar wind acceleration from anisotropic magnetohydrodynamic turbulence. *Astrophys. J.* 171 (suppl), 520-551 (2007)
35. Belin, A., Martens, P., Keppens, R. Coronal heating by resonant absorption: the effects of chromospheric coupling. *Astrophys. J.* 526, 478-493 (1999)
36. Withbroe, G., Noyes, R. Mass and energy flow in the solar chromosphere and corona. *Ann. Rev. Astron. Astro.* 15, 363-387 (1977)
37. Aschwanden, M., Winebarger, A., Tsiklauri, D., Hardi, P. The coronal heating paradox. *Astrophys. J.* 659, 1673-1681 (2007)
38. Rimmele, T., Recent advances in solar adaptive optics. Society of photo-optical instrumentation engineers conference series. 5490, 34-46 (2004)
39. Wger, A., von der Lhe, O., Reardon, K. Speckle interferometry with adaptive optics corrected solar data. *Astron. Astrophys.* 488, 375-381 (2008)
40. Jess, D. et al. High frequency oscillations in a solar active region observed with the Rapid Dual

Imager. *Astron. Astrophys.* 473, 943-950 (2007)

Supplementary Information is linked to the online version of the paper at www.nature.com/nature

Supplementary Figs. S1 to S8

Supplementary Tables S1 to S3

Supplementary Discussion

Supplementary Methods

Supplementary References (41-43)

Supplementary Movies S1 to S4

Acknowledgements RE acknowledges M. Kray for patient encouragement. The authors are also grateful to NSF, Hungary (OTKA, Ref. No. K83133), the Science and Technology Facilities Council (STFC), UK and the Leverhulme Trust for the support they received. Observations were obtained at the National Solar Observatory, operated by the Association of Universities for Research in Astronomy, Inc. (AURA), under agreement with the National Science Foundation. We would like to thank the technical staff at DST for their help and support during the observations and the Air Force Office of Scientific Research, Air Force Material Command, USAF for sponsorship under grant number FA8655-09-13085.

Author Contributions R.J.M (with D.K. and R.E.) performed analysis of observations. R.J.M, G.V., R.E. and M.S.R. interpreted the observations. D.B.J and M.M. performed all image processing. R.E. (Principal Investigator of the observations), M.M. and D.B.J. designed the observing run. All authors discussed the results and commented on the manuscript.

Author Information Reprints and permissions information is available at www.nature.com/reprints. The authors declare no competing financial interest. Correspondence and requests for materials should be addressed to R.E. (robertus@sheffield.ac.uk).

Supplementary material for

Observations of ubiquitous compressive waves in the Sun's chromosphere

R. J. Morton, G. Verth, D. B. Jess, D. Kuridze, M. S. Ruderman, M. Mathioudakis, R. Erdélyi*

* To whom correspondence should be addressed

Supplementary Figures

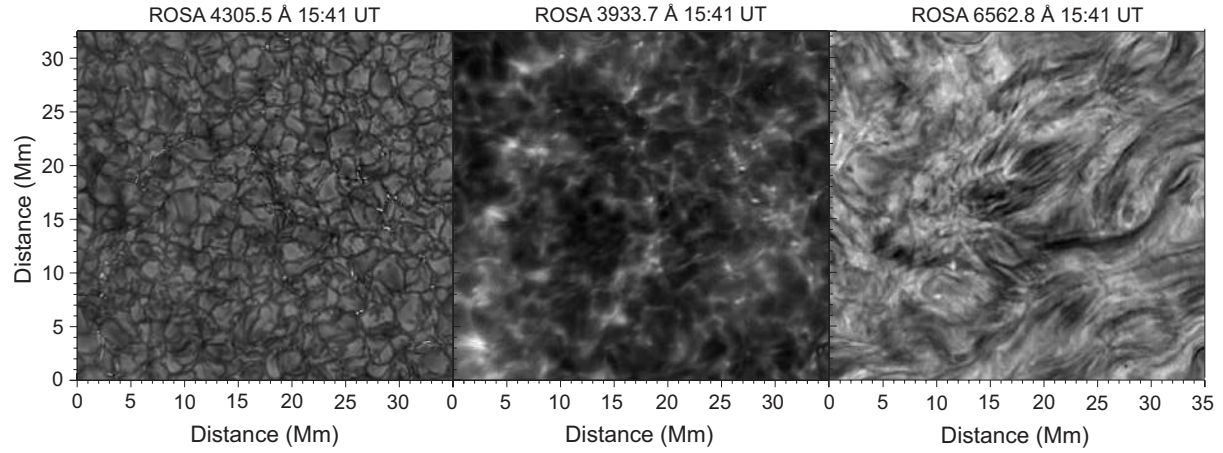


Fig. 6.— Supplementary Figure S1 **The photospheric magnetic field:** The **left** panel shows a ROSA G-band image which samples the lower photosphere. The bright points in the intergranular lanes highlight strong concentrations of magnetic flux. The **middle** panel is a co-temporal Ca II K image showing the upper photosphere/low chromosphere. The magnetic bright points seen in the G-band are also visible but have a more diffuse appearance. The **right** panel shows the corresponding H α image. All images are co-temporal and co-spatial.

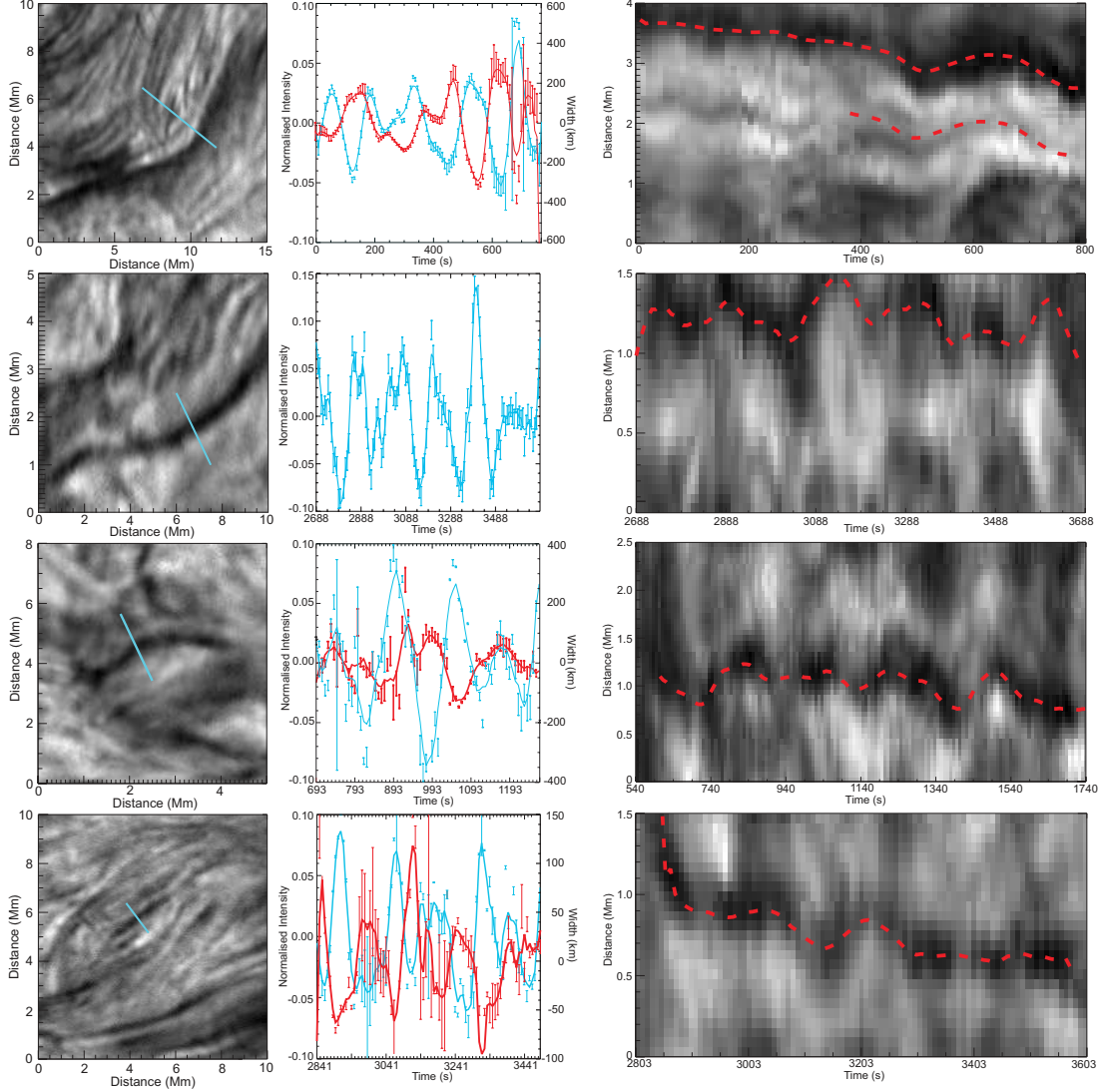


Fig. 7.— Supplementary Figure S2 **Concurrent wave modes**: **Left** panels show the $H\alpha$ chromospheric magnetic structures in which the waves were observed. The images, in descending order, are taken at $t = 380$ s, 3055 s, 770 s, 3095 s from the beginning of the data series. **Middle** panels display the structure’s intensity (blue) and width (red) as a function of time. The periodic behaviour in both intensity and width demonstrates the compressive behaviour identified as the fast sausage mode. **Right** panels show the observed fast kink wave. The given distances start from the top of the cross-cuts shown in the first panel. Details on each of the waves are given in Table S1 and how the periodic phenomenon are measured is described in Sections 2-4. Note, periodic phenomena shown in the second row have not been derived from a Gaussian fit. To obtain the transverse displacement of the structures axis we used the position of the minimum value of intensity for each cross-sectional flux profile. This technique has a larger error (± 50 km) than the Gaussian fit method. The value of minimum intensity is plotted in the second panel.

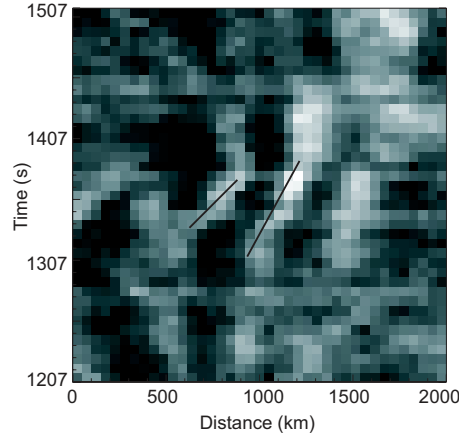


Fig. 8.— Supplementary Figure S3 **Measuring transverse motions:** A time-distance diagram displaying transverse wave motion. The black lines show typical linear fits to the transverse displacement. Gradients of the lines are the time-averaged velocity amplitude.

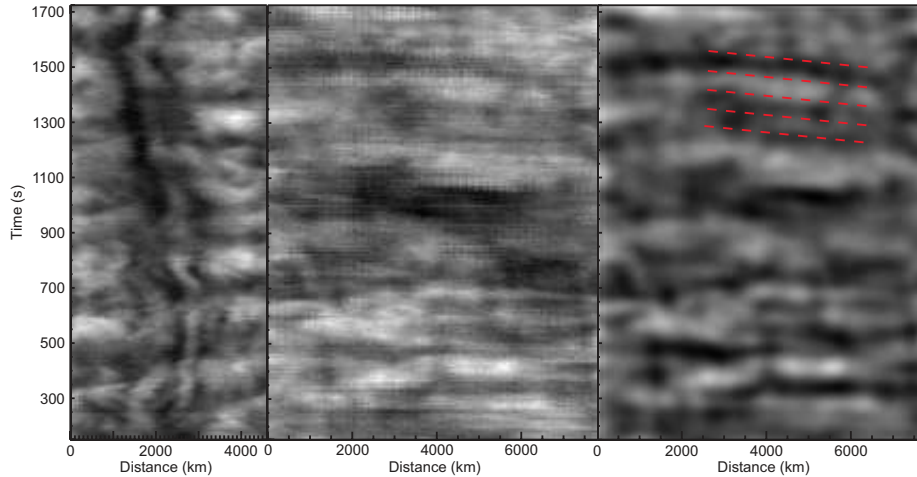


Fig. 9.— Supplementary Figure S4 **Comparison of methods:** The images shown here demonstrate the connection between the compressive disturbances identified with Gaussian fits and the periodic intensity phenomena seen in time-distance plots. The **left** hand image shows the time-distance plot of the chromospheric flux tube, discussed in Fig. 4, which demonstrated concurrent wave motions using the Gaussian fitting. The **middle** panel is a time-distance diagram for a cross-cut parallel to the flux-tube (see, Supplementary Fig. S5). The **right** panel displays the high pass filtered images of the middle panel, showing the periodic, propagating intensity disturbances (highlighted by the red dashed lines) which were previously identified with the Gaussian fitting. The measured propagation speed is $64 \pm 4 \text{ km s}^{-1}$.

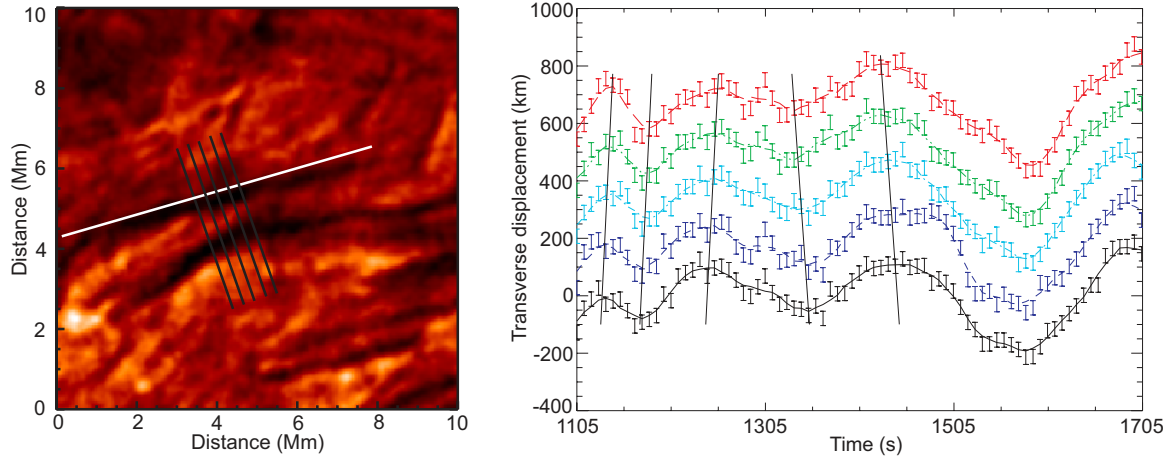


Fig. 10.— Supplementary Figure S5 **Measuring phase speeds:** The **left** panel shows the same chromospheric structure as that shown in Fig. 4. The white line shows the position of the parallel cross-cut used in the middle panel of Supplementary Fig. 7. The **right** panel shows the transverse motions from cross-cuts (shown in the left panel) at different positions along the chromospheric structure. The data points are obtained from the Gaussian fits and the error-bars are the one standard deviation error on the fit. The diagonal lines highlight the 87 km s^{-1} upwards (first set of lines) and 71 km s^{-1} downwards (second set) propagating waves. The visible shift in the signals confirms the results obtained from cross-correlation.

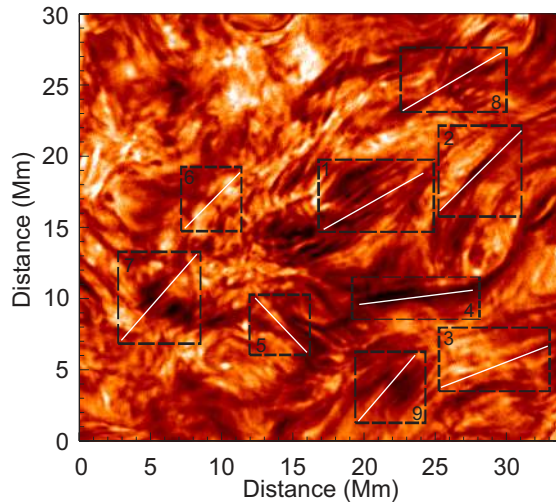


Fig. 11.— Supplementary Figure S6 **Regions showing fast propagating, periodic intensity perturbations:** A sub-region of the ROSA field of view. The boxes indicate areas in which evidence for fast propagating disturbances are found and the white lines show the cross-cut positions. The details of the observed oscillations are given in Supplementary Table S3.

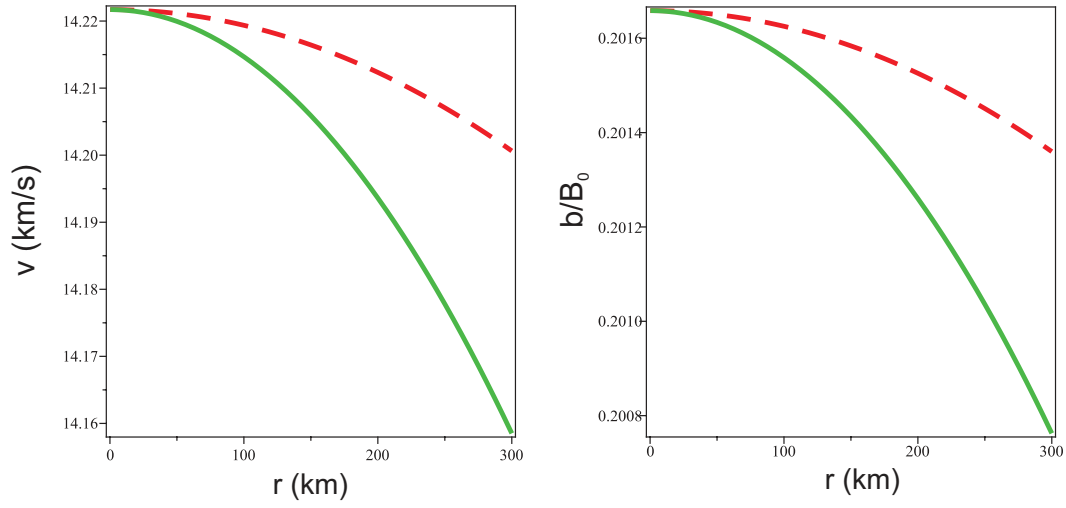


Fig. 12.— Supplementary Figure S7 **Theoretical amplitudes for the fast kink mode:** The **left** panel shows the amplitude of the velocity perturbations as a function of radius: v_r is the solid and v_θ is the dashed line. The amplitude of the magnetic field perturbations as a function of radius is demonstrated in the **right** panel. The values of the perturbations are normalised with respect to the equilibrium magnetic field, both of which cannot be measured directly: b_r is the solid and b_θ is the dashed line. The amplitude distributions are calculated for $c_{ph} = 70 \text{ km s}^{-1}$ and $k = 5 \times 10^{-4} \text{ km}$.

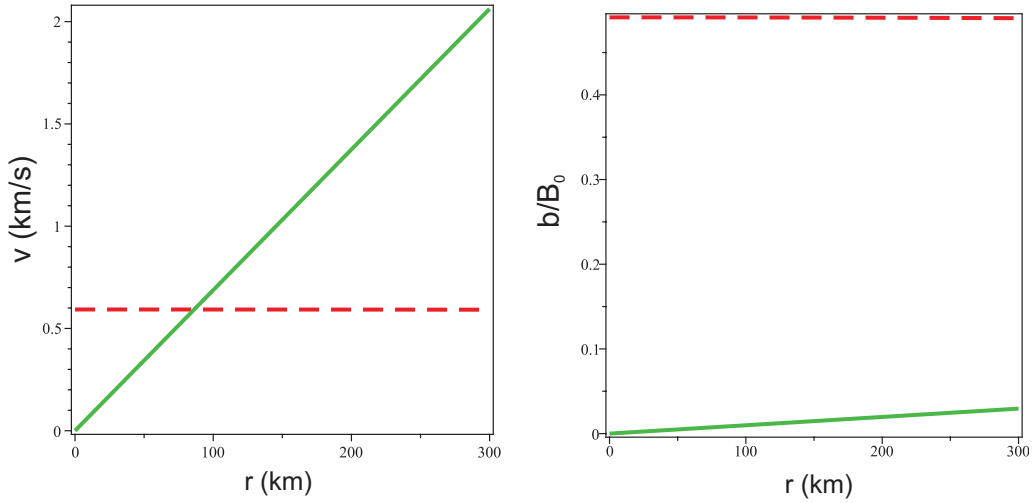


Fig. 13.— Supplementary Figure S8 **Theoretical amplitudes for the fast MHD sausage mode:** In the **left** panel v_r is the solid and v_z is the dashed line. In the **right** panel b_r is the solid and b_z is the dashed line. The values of the perturbations are normalised with respect to the equilibrium magnetic field, both of which cannot be measured directly. The amplitude distributions are calculated for $c_{ph} = 70 \text{ km s}^{-1}$ and $k = 4 \times 10^{-4} \text{ km}$. Note the different wave numbers of Figs. 4 and 5 that arises from the difference in observed periods and phase speeds of the two MHD wave modes.

Supplementary Tables

	Fast kink		Fast MHD Sausage	
	c_{ph} (km s ⁻¹)	Period (s)	c_{ph} (km s ⁻¹)	Period (s)
1	80 ± 20	180 ± 5	102 ± 15	135 ± 3
	58 ± 15			
2	92 ± 26	180 ± 5	110 ± 27	214 ± 6
3	58 ± 17	210 ± 3	87 ± 26	154 ± 5
4	-	182 ± 5	51 ± 12	203 ± 5

Supplementary Table S1. The measured properties of the observed waves in Supplementary Fig. S2. The numbers in the left column refer to the row in Supplementary Fig. S2. The wave labelled 1 displays both upward and downward propagating kink waves so two phase speeds are given.

Region	c_{ph} (km s ⁻¹)	Period (s)
1	135 ± 17	136 ± 10
	270 ± 135	130 ± 10
	78 ± 9	90 ± 10
2	86 ± 8	150 ± 10
	127 ± 12	150 ± 10
3	152 ± 15	140 ± 10
	122 ± 25	146 ± 10
	257 ± 61	148 ± 10
4	246 ± 80	121 ± 10
	82 ± 14	136 ± 10
5	48 ± 8	100 ± 10
	325 ± 81	100 ± 10
6	55 ± 5	116 ± 10
7	49 ± 4	162 ± 10
	84 ± 21	108 ± 10
8	57 ± 3	94 ± 10
9	58 ± 10	130 ± 10
	55 ± 4	192 ± 10

Supplementary Table S2. The measured properties of the fast propagating, periodic intensity perturbations. The regions are shown in Supplementary Fig. S6.

T	10,000 K
B_i	0.001-0.002 Tesla
ρ_i	$2\text{-}3 \times 10^{-10} \text{ kg m}^{-3}$
$v_A = B/\sqrt{\mu_0\rho}$	50 – 100 km s ⁻¹
$c_s = \sqrt{RT/\tilde{\mu}}$	10 km s ⁻¹

Supplementary Table S3. The typical chromospheric plasma parameters used for calculations of the wave energy. Here T is the plasma temperature (ref. 1,22,23), B is the magnetic field (ref. 28), ρ is the chromospheric density (refs. 1,22,23), v_A is the Alfvén speed, μ_0 is the magnetic permeability of free space, c_s is the sound speed, R is the gas constant and $\tilde{\mu}$ is the mean atomic weight. The subscript i refers to the internal quantities of the chromospheric structure.

Supplementary Discussion

Magnetic field structure

We provide additional ROSA data here in order to put our chromospheric observations in the context of the underlying magnetic field. The ROSA G-band (Supplementary Fig. S1 left panel) filter reveals a number of bright features in the inter-granular lanes. These features are frequently referred to as magnetic bright points (MBPs). The MBPs are common throughout the quiet Sun and usually correspond to strong magnetic field concentrations (~ 1 kGauss) (ref. 41). The MBPs highlight the super-granule network and are thought to correspond to open magnetic fields that reach into the corona (e.g., ref. 42). The Ca II K line samples the lower chromosphere but contains significant contributions from photospheric sources. The MBPs are also seen in the Ca II K images (Supplementary Fig. S1 middle panel), however their emission appears more diffuse. Previous observations (e.g., ref. 42) have demonstrated that fibrils and mottles (seen in H α) extend out from the strong flux concentrations.

Typically, flux tubes undergo expansion between the photosphere and chromosphere, hence this will reduce the magnitude of the magnetic field at chromospheric level compared to the photospheric value. Spectropolarimetric observations (ref. 28) have shown that the typical field strength from the chromosphere at the limb is of the order 10 – 40 G (0.001 – 0.004 Tesla). Using this value of magnetic field and typical values of density measured for chromospheric magnetic structures, we obtain estimates of Alfvén speeds (Supplementary Table S1) that are comparable to the phase speeds of the waves observed here.

We can set an upper limit on the area of the chromosphere occupied by open magnetic fields. If we assume each of the 300 chromospheric structures identified (Fig. 1) is formed along an open field line, i.e., protrudes into the corona, then the cross-sectional area of the observed structures would only cover approximately 4 – 5% of the observed chromosphere. This percentage is in agreement with estimates from previous observations (refs. 1, 36). Of course, not all the observed structures are open but this limit demonstrates only a small percentage of the chromosphere is open to the corona. This has implications for the wave-energy able to reach the corona from the chromosphere as discussed in the main paper.

We note that this estimate of connectivity between the chromosphere and corona is constrained by the current spatial resolution and the ability to resolve very fine structure. However, we suggest this upper bound would not change much even with improved resolution. At present, chromospheric structures with widths on the order of 100 km are reported. These occupy less than a tenth of the volume of structures with the median width of 360 km. Hence, a large number of unresolved structures need to exist to significantly alter the upper bound placed on the connection between the chromosphere and corona.

Explaining the compressive perturbations

The determination of which wave mode causes the observed periodic changes in intensity and cross-section is challenging. We begin by ruling out some of the possibilities.

- The observed modes cannot be slow modes as they propagate with speeds close to the local Alfvén speed. Slow modes propagate with phase speed close to the sound speed (ref. 25).
- An alternative option is that we detect a kink mode polarised in the line-of-sight in addition to the transverse displacement in the observational plane. This would, however, invoke a helical motion which has previously been tentatively reported in spicules. During a helical motion, both polarisations would have the same phase speed and period.

We use a narrowband H α filter, so Doppler shifts caused by the line-of-sight motion could cause an increase in intensity. However, the intensity would increase whether the flux tube was moving towards or away from the observer. Hence, if we had two oppositely polarised kink modes, the period for the change in intensity due to line-of-sight motion should be half the value of that measured for the observed transverse displacement. This is not the case. Secondly, this motion would not explain the change in the visible width of the tube. The entire flux tube would move towards or away from the observer at the same speed, leaving the visible width unaffected.

- The linear torsional Alfvén wave can also be ruled out as it is incompressible and does not cause a change in the flux tube width.
- The next possibility is that the observed change in intensity and width is a non-linear wave phenomenon.
 - Recent work (ref. 43) on propagating non-linear kink motions has shown that the non-linearity couples the kink motion to higher order (fluting) modes which can distort the cross-section of the flux tube. These higher order modes propagate with the same phase speed as the kink mode. Non-linear theory suggests that the higher order modes are relatively incompressible, which would leave the intensity perturbations unexplained.
 - The non-linear torsional Alfvén wave causes a compression of the cross-section and may alter the pressure inside the loop. This compression would have half the period of the non-linear Alfvén wave since compression would occur as the motion twists the magnetic surface in either direction. This implies the period of the non-linear Alfvén motion would be ~ 400 s. However, we can discard the torsional Alfvén wave as it would propagate with the *internal* Alfvén speed that is substantially smaller than the kink speed. In fact, our observations demonstrate just the opposite relation.

The crucial point from the observations is that the perturbations in width and intensity show a distinct phase relation. This suggests that the perturbations are related and can be attributed to

the same wave mode. Since we have already ruled the role Doppler effects play in the observed behaviour, we conclude here that the perturbations are genuinely a compressive phenomenon.

The only remaining choice is the fast sausage MHD mode. However, a trapped mode cannot propagate unless the dimensionless value ka satisfies (refs. 25, 27)

$$ka > j_0 \left(\frac{v_A^2}{v_{Ae}^2 - v_A^2} \right)^{1/2},$$

where the relationship is derived for low-beta plasma, and $j_0 \approx 2.4$ is the first zero of the Bessel function J_0 . The definition of a trapped mode is a wave that decays exponentially away from the wave guide.

To obtain the lowest possible cut-off value, we assume a cold, dense chromospheric structure embedded in a coronal plasma thus providing a maximum possible density contrast. Hence, $B_i \approx B_e$ and $\rho_i \gg \rho_e$, where $\rho_i = 3 \times 10^{-10} \text{ kg m}^{-3}$ (a typical value for chromospheric structures) and $\rho_e \sim 10^{-12} \text{ kg m}^{-3}$ (a typical coronal value), then the dimensionless wavenumber has to satisfy $ka > 0.2$. The wavenumber for the observed oscillation in Fig. 4 is $k \approx 3.8 \pm 1.0 \times 10^{-4} \text{ km}^{-1}$ and $a = 200 \pm 50 \text{ km}$, giving a predicted value of $ka \sim 0.08 \pm 0.03$. Even with these extreme density contrast values the observed ka is still less than the cut-off value. Therefore, we are confident that we observed a leaky fast sausage MHD wave.

Leaky modes differ from trapped modes in that their wave energy is radiated away from the tube as the wave propagates, typically resulting in short lifetimes on the order of a period. Because we see multiple periods of a propagating mode this may suggest a continuous driver. Since the wave energy leaks from the tube, the surrounding chromospheric structures should experience coherent oscillatory behaviour, which is seen in Supplementary Movies S3 and S4, where a number of chromospheric magnetic structures appear to support fast propagating disturbances at approximately the same time.

Supplementary Methods

Measuring the period of the waves

The period of the observed oscillatory phenomena is measured using wavelet analysis. The observed oscillation in either central position/intensity/width is subject to a wavelet transform and the wavelet component with the greatest power is identified as the period of the oscillation. The wavelet decomposes the signal at certain frequency intervals. The size of the wavelet scales used means there is a 20 s uncertainty in the determining the period. The error is reduced by making multiple measurements of the period from different cross-cuts from the Gaussian fits (see, e.g. Supplementary Table 1). For the slits placed parallel to the fine structure (see, e.g. Supplementary Table 2), we measure the period of the oscillation in intensity in five columns in each cross-cuts through the oscillations and take the average value. The error on the average period is then the reduced value of $\sim 10 \text{ s}$.

Calculating the wave energy

Here we demonstrate how the wave energy flux can be calculated for a waveguide model of the chromosphere. The waveguide model attempts to take into account the observed fine-structure of the chromosphere.

The energy flux of the observed waves can be estimated from the measured amplitudes and phase speeds. The first assumption is that the chromospheric magnetic structures are over-dense homogeneous cylindrical magnetic waveguides embedded in an ambient plasma. To reduce the complexity of the calculations, here we use linear theory to relate the amplitudes of perturbations of different quantities. The waveguide supports an infinite set of orthogonal MHD wave eigenmodes. In the non-linear theory (ref. 43), eigenmodes strongly interact and cannot be separated. Linear theory provides a good first approximation of the wave energy flux.

We are interested in the energy flux at a particular height in the solar atmosphere, so we neglect the variation of background quantities along the waveguide and assume that the plasma is homogeneous in the radial direction inside. Using cylindrical coordinates (r, θ, z) and assuming that the perturbations of all quantities are proportional to $\exp -i(\omega t - n\theta - kz)$, we obtain the following set of equations describing the dependence of perturbations on the radial coordinate r (see, e.g., ref. 24)

$$\begin{aligned}
 v_r &= -A \frac{\omega^2 - k^2 c_s^2}{m_0^2 \omega^2} \frac{dJ_n(m_0 r)}{dr}, & v_\theta &= Ai \frac{\omega^2 - k^2 c_s^2}{m_0^2 \omega^2} \frac{n}{r} J_n(m_0 r), \\
 v_z &= -Ai \frac{k c_s^2}{\omega^2} J_n(m_0 r), & b_r &= -\frac{k}{\omega} B_0 v_r, \\
 b_\theta &= \frac{k}{\omega} B_0 v_\theta, & b_z &= Ai \frac{\omega^2 - k^2 c_s^2}{\omega^3} B_0 J_n(m_0 r).
 \end{aligned} \tag{S1}$$

Here, $\mathbf{v} = (v_r, v_\theta, v_z)$ are the velocity perturbations, $\mathbf{b} = (b_r, b_\theta, b_z)$ are the magnetic field perturbations, ω is the frequency of the oscillation, k is the wavenumber, J_n is the Bessel function of the first kind, n refers to the angular wave number (or mode number) and A is some constant which is used to scale the amplitudes. Further,

$$m_0^2 = \frac{(\omega^2 - v_A^2 k^2)(\omega^2 - c_s^2 k^2)}{(c_s^2 + v_A^2)(\omega^2 - c_T^2 k^2)},$$

where $c_T = c_s v_A / \sqrt{(c_s^2 + v_A^2)}$ is the tube speed. The use of J_n is only valid as long as $c_T < c_{ph} < \min(c_s, v_A)$ or $\max(c_s, v_A) < c_{ph}$, which guaranties that $m_0^2 > 0$. In this case the wave is referred to a body mode. If these conditions are not satisfied, and $m_0^2 < 0$, then we have to substitute $I_n(|m_0| r)$ for $J_n(m_0 r)$. In this case the wave is referred to as a surface wave.

Fast kink wave

Using the set of Equations (S1) with $n = 1$ and the estimates for the plasma parameters, we determine the amplitudes of the perturbations as a function of radius.

In Supplementary Fig. S7 we show the amplitude profiles of v_r , v_θ , b_r and b_θ as a function of radius. The profiles are shown for a waveguide of radius 300 km, which is typical for chromospheric structures (see, Fig. 1). For the plots in Supplementary Fig. S7 a phase speed $c_{ph} = 70 \text{ km s}^{-1}$ is used and the wavenumber $k = 5 \times 10^{-4} \text{ km}^{-1}$ is calculated using the phase speed and the typical periods of the kink oscillations, $P = 180 - 200 \text{ s}$. The amplitudes vary only by $< 1\%$ across the internal plasma of the waveguide.

Next, we assume that the observed waves are propagating in a cold plasma, i.e., the plasma- β is small, where β is the ratio of the gas pressure to the magnetic pressure. For the given values of plasma parameters $\beta < 0.03$ (see, Supplementary Table S3), so this approximation is valid. The equation for the time averaged energy flux is then given by

$$\langle E \rangle = \frac{1}{4} c_{ph} \left[\rho_i (v_r^2 + v_\theta^2 + v_z^2) + \frac{1}{\mu_0} (b_r^2 + b_\theta^2 + b_z^2) \right]. \quad (\text{S2})$$

The first set of terms in the squared brackets is the kinetic energy flux, while the second set relates to the magnetic energy flux. This equation requires that we know the amplitudes of the perturbations. However, we have measured the time-averaged value of the velocity for the transverse motions. Hence, to calculate the time-averaged energy flux using the measured velocity we use

$$\langle E \rangle = \frac{1}{2} c_{ph} \left[\rho_i (\langle v_r \rangle^2 + \langle v_\theta \rangle^2 + \langle v_z \rangle^2) + \frac{1}{\mu_0} (\langle b_r \rangle^2 + \langle b_\theta \rangle^2 + \langle b_z \rangle^2) \right]. \quad (\text{S3})$$

For the fast kink wave the v_z and b_z perturbations are sufficiently small and may be neglected. By substituting the calculated average values of the perturbations into the energy flux equation, we obtain a range of the energy flux for the transverse mode, $\langle E_k \rangle = 4300 \pm 2700 \text{ Wm}^2$. Here we have used $\langle v_r \rangle = 5 - 10 \text{ km s}^{-1}$ and the range of values given in Supplementary Table S3. We note the energy of the modes is evenly distributed between the magnetic and kinetic terms.

Fast MHD sausage mode

To obtain the perturbation amplitudes for the fast MHD sausage modes, we set $n = 0$ in the set of Equations (S1). This decouples the v_θ and b_θ perturbations from the other perturbations, hence, the sausage mode has no azimuthal components. To determine the amplitude profiles we set the amplitude at the tube boundary equal to the value estimated from the observations. Note, the v_r estimated for the fast MHD sausage mode would be the amplitude and not the time-averaged value.

The calculated amplitude profiles for the fast MHD sausage mode are shown in Supplementary Fig. S6. The v_r and b_r perturbations are zero at the centre of the waveguide and reach a maximum at its boundary. On the other hand, the amplitudes of the v_z and b_z perturbations are approximately constant across the waveguide radius. It also worth noting that the amplitudes of the b_z perturbations for the fast MHD sausage mode are large compared to the b_r components.

The equation for the time-averaged energy flux for the fast MHD sausage mode in a low- β plasma is

$$\langle E_s \rangle = \frac{1}{4} c_{ph} [(v_r^2 + v_z^2) + (b_r^2 + b_z^2)]. \quad (\text{S4})$$

The estimated amplitudes for v_r are small, e.g. when compared to the velocity amplitudes of the fast kink mode, and the dominant terms are due to the magnetic energy flux. The estimated wave energy flux for the fast sausage mode is in the range $E_s = 11700 \pm 3800 \text{ Wm}^{-2}$ for velocity amplitudes of $1.5 - 2 \text{ km s}^{-1}$ and the range of values given in Supplementary Table S3.

Supplementary References

41. Berger, T., Title, A., On the relation of G-band bright points to the photospheric magnetic field. *Astrophys. J.* **533**, 449-469 (2001)
42. Rutten, R. J., Observing the solar chromosphere. *The physics of chromospheric plasmas ASP conference series*, Ed. P. Heinzel, I. Dorotovič, R. J. Rutten. **368**, 27 (2007)
43. Ruderman, M. S., Goossens, M., Andries, J. Nonlinear propagating kink waves in thin magnetic tubes. *Phys. Plasmas* **17**, (2010)